Catalysis Science & Technology

Accepted Manuscript

ROYAL SOCIETY OF CHEMISTRY

www.rsc.org/catalysis

Selective catalytic reduction over the size-tunable rutile TiO_2 nanorod microspheres supported CeO_2 catalysts

Kai Cheng, Weiyu Song[†], Ying Cheng, Jian Liu*, Zhen Zhao, Yuechang Wei

（State Key Laboratory of Heavy Oil Processing, China University of Petroleum, Beijing
102249, China）

* Corresponding author: Email address: liujian@cup.edu.cn

†: This author has equal contribution as the first author

Postal Address: 18# Fuxue Road, Chang Ping District, Beijing, 102249, China,

Tel: 86-10-89732326, Fax: 86-10-69724721

Abstract

The size-tunable 3D rutile TiO_2 spheres consisting of nanorod were controllably synthesized by adjusting the precursor hydrolysis rate. CeO_2 nanoparticle was supported on TiO_2 to prepare a series of Ce/Ti catalysts via incipicent-wetness impregnation method. The catalytic activity tests showed that the hierarchical rutile TiO_2 microspheres with 1 μm size consisting of nanorods supported CeO_2 showed excellent activity and high N_2 selectivity in a wide temperature range. The novel morphology of TiO_2 nanostructures exhibits a strong interaction with CeO_x speices, enhancing its dispersion. The excellent catalytic activity should be mainly attributed to the enriched surface oxygen species, abundant surface acidity and high reducibility. The presence of enriched surface oxygen vacancies could facilitate the formation of active NO_2 and bidentate nitrate species, leading to remarkable SCR performances. This was confirmed by the in-situ DRIFTS investigations.

Key words: SCR; TiO_2 microspheres; Controllable synthesis; Cerium oxide; NO reduction

1. Introduction

Nitrogen oxides (NO_x) emitted from automobile exhaust gases and the industrial combustion of fossil fuels are the major air pollutants. They cause environmental problems such as acid rain, photochemical smog, haze weather and ozone depletion.[1, 2] Selective catalytic reduction (SCR) of NO_x with NH_3 is nowadays the most promising technology for eliminating NO_x. V_2O_5-WO_3/TiO_2 has been widely used as an industrial catalyst, which exhibit excellent catalytic performance in the temperature range of 300-400 °C. However, there are still some drawbacks in these catalyst systems such as high working temperature, toxicity of vanadium species and low N_2 selectivity at high temperatures.[3-5] Many efforts have been made to develop an environmentally friendly SCR catalyst to replace V-based catalysts and several catalyst systems have been developed. For example, Cu- and Fe-exchanged zeolite catalysts show excellent catalytic performances for the SCR of NO_x by NH_3.[6, 7] Other nontoxic transition metal oxide-based catalysts have also been extensively studied as potential candidates, such as Ce-Zr-based,[8, 9] Ce-W-based,[10, 11] Ce-Mn-based[12] and Fe-Ti-based catalysts.[13, 14]

Ceria has attracted increasing attention due to its superior oxygen storage capacity and high redox ability when shifting between Ce^{4+} and Ce^{3+}. He et al.[15] reported that Ce/Ti catalyst exhibited the excellent NO reduction activity and high N_2 selectivity in the medium temperature range. However, it is reported that traditional Ce/Ti catalyst showed the poor SO_2 resistance.[16] In order to widen the temperature windows and improve SO_2 resistance of Ce/Ti based catalysts, many works were paid attention to doping the modification agents to Ce/Ti catalyst, such as W,[17] Mn,[18] Zr[19] etc. The other way is to develop the new preparation method of CeO_2-TiO_2 catalyst, such as sol-gel method,[9] supercritical water synthesis[20] and flame-spray synthesis.[21] It is claimed that the high NH_3-SCR activity and strong SO_2 resistance are always related to the close interaction between cerium and titanium components and the highly dispersed CeO_2 nanocrystallite.

Recently, considerable efforts have been devoted toward understanding the correlations between the morphology of nanomaterials and their catalytic activities of NH_3-SCR reaction. Among materials with controlled shapes, titania/titanate nanocrystals are of particular interest because of their unique electronic and optical properties. For example, novel titanate nanotube confined CeO_2 catalysts were designed and such catalysts showed a remarkable resistance to alkali metal poisoning in deNOx application due to confining alkali metal ions in the interlayer through ion exchange.[22] Cu species supported on titanate-derived TiO_2 nanotubes were also developed. It was shown that Cu species are more highly dispersed and dissolved into TiO_2 and are more active in catalyzing NO reduction.[23] In addition, Gao et al.[24] used TiO_2 microspheres as support to synthesize V_2O_5-WO_3/Fe_2O_3/TiO_2 catalysts, and such catalysts exhibited the excellent catalytic performance of NH_3-SCR, but the resistances to SO_2 are still needed to be enhanced.

The interaction between CeO_2 and TiO_2 support will change when TiO_2 nanorod was assembled to the orderly microspheres. In this study, size-tunable TiO_2 nanorod microspheres were synthesized by one-pot hydrothermal method and employed as catalyst supports. CeO_2 was added as the active species component to get Ce/Ti catalysts with the excellent catalytic performances and improved SO_2 and H_2O resistance for NH_3-SCR. Ce/P25 catalyst was also prepared by an impregnation method for comparison. The effects of morphology on the surface properties of the catalysts were also studied using N_2-physisorption, XRD, SEM, TEM, H_2-TPR, XPS, Py-IR and in-situ DRIFTS. Finally, the mechanistic of the promoting effect and the catalytic reaction was discussed.

2. Experimental

2.1. Catalyst preparation

TiO_2 microspheres assembled by single crystalline rutile TiO_2 nanorods were synthesized by one-pot hydrothermal treatment[25]. In a typical synthesis, 20 mL of n-hexane, a few milliliters of distilled water, and 2 mL of concentrated hydrochloric acid were mixed in a beaker, and then 4 mL of TBT was added dropwise to the mixture under magnetic stirring. After 15 minutes the mixed solution was transferred into a Teflon-lined autoclave of 50 mL capacity. Subsequently, the autoclave was sealed and treated at 180 ^{o}C for 4 h, followed by natural cooling to room temperature. Afterward, the products were collected by centrifugation, and washed with ethanol three times. Finally, the material was dried at 80 ^{o}C for 12 h and then annealed in air at 500 °C for 5 h. The catalysts (CeO_2 loading was 10 wt.%) were prepared by impregnating TiO_2 with a proper amount of cerium nitrate ($Ce(NO_3)_3 \cdot 6H_2O$) solution. The samples were dried at 110 °C for 12 h followed by calcination at 500 °C in air for 3 h. Finally, the catalysts were crushed and sieved to 20-40 mesh size. For the reference catalyst (Ce/P25), TiO_2 from Degussa P-25 was used as support and prepared in the same way used for the other catalyst. For the sake of the brevity, the catalysts were denoted as Ce/Ti-*x*, Where, *x* represented the volume ratio of titanium n-butoxide (TBT) to H_2O, respectively, and x = 1, 2, 3, 4.

In such a synthetic process, the reaction between TBT and HCl would firstly form a six-coordinated complex, $Ti_6O_6Cl_6(OBu)_6$ (R1). Then, H_2O could further react with the complex of $Ti_6O_6Cl_6(OBu)_6$ to produce $Ti_6O_6Cl_6(OBu)_{6-x}(OH)_x$ ($0 \le x \le 6$) (R2), where *x* were associated with the acidity. The subsequent condensation reaction may form the titania nuclei at the initial stage during the hydrothermal treatment.

$$6Ti(OBu)_4 + 18HCl \rightarrow Ti_6O_6Cl_6(OBu)_6 + 6BuOH + 12BuOCl + 6H_2O \quad (R1)$$

$$Ti_6O_6Cl_6(OBu)_6 + xH_2O \rightarrow Ti_6O_6Cl_6(OBu)_{6-x}(OH)_x + xBuOH \quad (R2)$$

Then, titania nanorods were formed due to the strong adsorption of Cl^- onto the (110) plane. Large amount of nanorods were self-assembled to radially spherical structures to minimize the surface area and reduce the system energy. The hydrolysis and condensation rate of TBT were controlled by adjusting the volume ratios of TBT to H_2O. The hydrolysis rate of TBT was too fast to form TiO_2 microspheres when TBT/H_2O was below 1, which would lead to only disordered nanorods being formed. With increasing TBT/H_2O to 2, TiO_2 nanorods had not yet completely grown into TiO_2 microspheres, and only small microspheres were formed. Further increasing TBT/H_2O to 4, TiO_2 microspheres had been formed completely with the diameter of 4 μm. The interface between two immiscible solvents may provide a suitable environment for self-assembly. A proposed mechanism for the formation of the nanorod microspheres is illustrated in Figure 1.

2.2. Physical and chemical characterization

The crystal structures of the fresh catalysts were determined with a powder X-ray diffractometer, using Cu Ka (λ = 0.1542 nm) radiation combined with a nickel filter operating at 40 kV and 10 mA (Shimadzu, Japan). The diffractometer data were recorded for 2θ values from 10^o to 80^o at a scanning rate of 4^o/min. The patterns were compared with ICDD files for phase identification.

The Brunauer-Emmett-Teller (BET) surface areas were measured by N_2 adsorption and desorption (Quantachrome Instruments, USA). The samples were degassed at 200 ^oC for 12 h.

The surface morphology of the catalyst was observed by field emission scanning electron microscopy (SEM) on a Quanta 200F instruments using accelerating voltages of 5 kV, in combination with an EDAX genesis 4000 energy-dispersive X-ray spectrometer (EDX). Samples for SEM was dusted on an adhesive conductive carbon belt attached to a copper disk and were coated with 10 nm Au prior to measurement.

TEM images were carried out using a JEOL JEM-2100 electron microscope equipped with a field emission source at an accelerating voltage of 200 kV. Drops of the suspension were applied, and after drying, the fine particles were well dispersed on a copper grid coated with carbon. The elemental local mapping were acquired by energy-dispersive spectroscopy (EDS) using a Tecnai F20 electron microscope equipped with a STEM unit and a CCD detector.

X-ray photoelectron spectroscopy (XPS) spectra were recorded with a standard AlK source (1486.6 eV) working at 350 W (XSAM800, Kratos Analytical company, UK). The working pressure was less than 2×10^{-7} Pa. The spectrometer was calibrated by assuming the binding energy (BE) of Au $4f_{7/2}$ line to lie at 84.0 eV with respect to the Fermi energy level. Binding energies of Ce 3d and O 1s were calibrated using C 1s peak (BE = 284.8 eV) as standard.

Temperature programmed reduction with H_2 (H_2-TPR) experiments were performed on the Quantachrome Instruments of Autosorb IQ. 100 mg sample was pretreated under Ar by calcination at 300 ^oC for 1 h and subsequently cooled to 30 ^oC. Afterwards, 10% H_2/Ar flow (60 ml·min^{-1}) was passed over the catalyst bed while the temperature was ramped from 30 to 800 ^oC at a heating rate of 10 ^oC min^{-1}.

The nature of the acid sites of the catalysts was determined by pyridine-IR (Py-IR) on a MAGNAIR 560 FT-IR instrument with a resolution of 4 cm^{-1}. The samples were dehydrated at 500 ^oC for 5 h under a vacuum of 1.33×10^{-3} Pa, followed by the adsorption of purified pyridine vapor at room temperature for 20 min. The system was then degassed and evacuated at different temperatures, and Py-IR spectra were recorded.

In-situ DRIFTS were recorded using a thermo Nicolet IS50 spectrometer, which was equipped with a high temperature environmental cell fitted with ZnSe window and an MCT detector cooled with liquid N_2. The catalyst was loaded in the Harrick IR cell and heated to 400 °C under N_2 at a total flow rate of 50 ml·min^{-1} for 60 min to remove adsorbed impurities. A background spectrum was collected under a flowing N_2 atmosphere and was subtracted from the sample spectra. The DRIFTS were recorded by accumulating 32 scans with a resolution of 4 cm^{-1}.

2.3. Activity measurements

The activity tests of various catalysts for NH_3-SCR of NO were carried out in a fixed bed quartz reactor (i.d. 6 mm). The feed gas mixture consisted of 1000 ppm of NO, 1000 ppm of NH_3, 100 ppm of SO_2 (when used), 5vol.% of H_2O (when used), 3vol.% of O_2 and N_2 balanced gas. A total flow rate of 500 ml·min^{-1} was maintained for all experiments. 0.4 g catalysts were used for evaluation in the reaction. The concentration of NO_x (NO_x = NO + NO_2) in the inlet and outlet gas was measured by a flue gas analyzer (Model-4000VM, SIGNAL International Ltd., UK). Meanwhile, the concentration of NH_3 and N_2O were measured by a FTIR spectrometer (Nicolet IS50). All catalysts were kept on stream at each temperature for 30 min. NO_x conversion was defined as follow:

$$\mathrm{NO_x\ conversion}\ (\%) = \frac{\mathrm{NO_{x\,(inlet)}} - \mathrm{NO_{x\,(outlet)}}}{\mathrm{NO_{x\,(inlet)}}} * 100\% \qquad (1)$$

N_2 selectivity in SCR reaction was calculated from Eq. (2).

$$\mathrm{N_2\ Selectivity}\ (\%) = \frac{2[\mathrm{N_2}]_{out}}{2[\mathrm{N_2}]_{out} + 2[\mathrm{N_2O}]_{out} + [\mathrm{NO_2}]_{out}} * 100\% \qquad (2)$$

3. Results and discussion

3.1. SCR performance

Fig. 2a shows the results of NO_x conversion in NH_3-SCR reactions over Ce/P25 and Ce/Ti-*x* catalysts in the temperature range of 200-450 °C. A significant difference on the catalytic activity was observed. Among all the catalysts, Ce/Ti-2 catalyst exhibited the highest

NO_x conversion and the widest temperature window of catalytic activity for the removal of NO_x among Ce/Ti-*x* catalysts, followed by Ce/Ti-1, Ce/Ti-3 and Ce/Ti-4 was least active. Compared with Ce/P25, Ce/Ti-2 catalyst also showed the higher NO_x conversion. However, the temperature window of Ce/Ti-1 shifted towards low temperature range to a certain extent compared with Ce/P25 catalyst. Furthermore, it should be noted that NO_x conversion decreased at 350 ^oC or higher temperature, which was due to the occurrence of the unselective oxidation of NH_3. Moreover, N_2 selectivity of Ce/P25 and Ce/Ti-*x* catalysts, which were similar each other in the whole temperature range, was above 90%. These catalysts were further characterized to discuss the structure-activity relationship in NH_3-SCR reaction.

3.2. SO_2 and H_2O resistance

The catalytic performances of SCR catalysts could be affected in the presence of SO_2 and H_2O. The influence of H_2O on the NH_3-SCR activity of Ce/P25 and Ce/Ti-2 catalysts at 300 ^oC was investigated and the results were shown in Fig. 3a. When 5% H_2O was introduced into the simulated exhaust gases at 300 ^oC, NO_x conversions decreased slightly and then remained constantly during the activity test for 10 h. These results indicated that water vapor inhibited the catalytic activity slightly at 300 ^oC, which may be attributed to the competitive adsorption between H_2O and NH_3 on the acid sites. After H_2O was cut off, NO_x conversions were recovered at 300 ^oC. The effect of SO_2 on the NH_3-SCR activity of Ce/P25 and Ce/Ti-2 catalysts at 300 ^oC was investigated and the results were shown in Fig. 3b. When 100 ppm SO_2 was introduced into the stream at 300 ^oC, NO_x conversion over Ce/Ti-2 catalyst decreased slightly and remained about 81% during the activity test for 10 h. This result indicated that SO_2 inhibited the catalytic activity slightly at 300 ^oC. After SO_2 was eliminated from the feed gas, NO_x conversion was restored to the initial value and then remained constantly for Ce/Ti-2 catalyst. By contrast, the presence of SO_2 in the feed gas induced a significant decrease of NO_x conversion over Ce/P25 catalyst from 90% to 66%, which might be related to the deposition of high thermally stable $Ce(SO_4)_2$ and $Ce_2(SO_4)_3$ on the surface of the catalyst and blocking the active sites.[16] After SO_2 was cut off, NO_x conversion was not recovered.

NH_3-SCR activity in the presence of both H_2O and SO_2 over Ce/Ti-*x* and Ce/P25 was also investigated and the results were shown in Fig. 3c. NO_x conversion over Ce/Ti-2 catalyst decreased to about 79% and then remained stably after 5% H_2O and 100 ppm SO_2 were introduced together. NO_x conversion increased to about 90% after the mixture of H_2O and SO_2 were cut off. By contrast, the activity on Ce/Ti-3 and Ce/Ti-4 catalysts decreased sharply under the coexistence of 100 ppm SO_2 and 5% H_2O. Nevertheless, the removal of H_2O and SO_2 from simulated exhaust gases raised the NO_x conversion on Ce/Ti-3 and Ce/Ti-4 catalysts to a certain extent, and NO_x conversion remained 80% and 75%, respectively. From the above results, it could be seen that Ce/Ti-2 catalyst gave the best resistance to SO_2. According to the results of H_2-TPR and XPS, the adsorption of SO_2 on the surface of Ce/Ti-2 catalyst due to the strong interaction between ceria and titania and different Ce species on different catalyst surface.

3.3. The results of XRD

Fig. 4 shows XRD patterns of Ce/Ti-*x* catalysts. All the diffraction peaks are assigned to the rutile phase of TiO_2, indicating perfect crystallinity, in particular in the (110) plane. The crystallite sizes of the primary TiO_2 are determined to fall in the 23-26 nm range, as estimated from the full width at half maximum of the (110) peak using the Scherrer equation. All the primary crystallites have a similar size, implying that the primary nanorods are not appreciably affected by the volume of distilled water. In addition, the peak attributed to fluorite CeO_2 (at 28.0^o) is very close to the peak attributed to rutile TiO_2 (27.6^o) and the peak intensity of rutile TiO_2 may be too strong to overlap that of fluorite CeO_2. They were not distinguished from current XRD patterns. Thus, the structures of CeO_2 on Ce/Ti-*x* catalysts should be investigated by the subsequent characterization.

3.4. The results of BET

Fig. 5 shows the nitrogen adsorption-desorption isotherms results of Ce/P25 and Ce/Ti-*x* catalysts. The textural and structural properties of all catalysts are shown in Table 1. The isotherms for Ce/P25 and Ce/Ti-x catalysts are similar to typical type IV isotherms. As shown in Table 1, Ce/Ti-2 and Ce/Ti-1 catalysts exhibit the relatively high special surface areas and micro-pore volume, while Ce/Ti-4 and Ce/Ti-3 catalysts show low surface areas of 32.6 and 34.7 $m^2 \cdot g^{-1}$, respectively. This phenomenon may be due to their special morphologies, which is in accordance with Rui et al. report.[25]

3.5. The results of SEM

Fig. 6 shows SEM images of Ce/Ti-*x* catalysts and EDX analyses for Ce/Ti-2 catalyst. Firstly, titania nanorods were formed due to the strong adsorption of Cl^- onto the (110) plane. Fig. 6a_1-a_3 shows the morphology of Ce/Ti-1 obtained from the volume ratio of TBT to H_2O at 1. Most of the spherical structures were not formed and disordered nanorods were formed. The length of nanorod is about 230 nm. Secondly, large amount of nanorods were self-assembled to radially spherical structures. When the volume ratio of TBT:H_2O = 2, three dimensional (3D) hierarchical rutile TiO_2 spheres consisting of nanorods were formed and the sphere size was about 1 μm (Fig. 6b_1-b_3). It can be observed that the spheres are well dispersed and almost no abnormal aggregations exist. With the increasing of the proportion of TBT:H_2O to 3, 3D hierarchical rutile TiO_2 spheres consisting of nanorods were still remained. However, the sphere size increased to 2 μm and the nanorod building units tended to aggregate (Fig. 6c_1-c_3). On further increasing the volume ratio of TBT:H_2O to 4, the nanorod building units seemed such aggregation that only rutile TiO_2 spheres were observed and the sphere size further increased to 4 μm (Fig. 6d_1-d_3). In addition, SEM results confirmed that size-tunable TiO_2 nanorod microspheres structures are still preserved after being calcined for 4 h. Fig. 6e shows SEM image and EDX analyses for Ce/Ti-2 catalyst. The mass fraction of CeO_2 was 10.86 wt.% from EDX results, which is in good agreement with the initial loading amounts.

3.6. The results of TEM

Ce/Ti-2 catalyst was composed of loosely packed nanorods, and the microstructure of the microspheres was further examined by TEM (Fig. 7a-f). It is seen that nanorods with a length of several hundred nanometers radiated from the center and assembled the hierarchical spherical structure. From high-resolution TEM images (Fig. 7d and 7e), the nature of the nanorods is clearly observed. Based on interplanar distance analysis, two phases have been identified in the crystalline regions of the sample: rutile TiO_2 and cubic CeO_2, which is consistent with the XRD results. CeO_2 particles possess an extended interface with the rutile TiO_2 nanorods suggesting the growth of CeO_2 out of TiO_2 structure. Contrary to the typical cubic morphology of CeO_2 particles, these particles are clearly round-shaped, which suggests a great fraction of defects, likely induced by the underlying rutile TiO_2 nanorod structure. CeO_2 particles probably grew layer by layer. Johnston-Peck et al. [26] investigated theoretically and experimentally fluorite cubic CeO_2 grown on anatase and observed that the elongated islands of CeO_2 similar to those observed in Figure 7d grow epitaxially (i.e., layer by layer) on TiO_2 due to the strain generated by the lattice mismatch. This form facilitates elastic relaxation of the stress. In addition, CeO_2 was not detected in the form of isolated crystalline particles in the TEM images, confirming the amorphous nature and the strong dependence on the TiO_2 structure as explained above.

In order to further study the active specie dispersion, high-angle annular dark-field scanning transmission electron microscopy (HAADF STEM) was employed evaluate the dispersion of CeO_2 over the Ti-2 and P25 supports. Fig. 7c and d show EDX mapping images of Ce/Ti-2 and Ce/P25 catalysts. For Ce/Ti-2 catalyst, CeO_2 (green dots/rods) was observed highly dispersed over the Ti-2 support, which is due to its nanorod structure. In contrast, Ce/P25 catalyst revealed the aggregation of green dots/rods, showing a comparatively poor dispersion of CeO_2. The results reveal the advantage of the nanorod structure is beneficial to the highly dispersed Ce species, which might give rise to superior catalytic performance in SCR application.

3.7. The results of H_2-TPR

To gain a better understanding of the redox properties of the catalysts, H_2-TPR detection of Ce/Ti-*x* and Ce/P25 catalysts were carried out. Fig. 8 shows H_2-TPR profiles of the Ce/Ti-*x* and Ce/P25 catalysts. In a simple approach, they generally reveal three hydrogen consumption peaks at approximately 410, 516 and 705 ^oC (denoted as α, β and γ in Table 2, respectively). The peaks at 410 and 516 ^oC are attributed to the reduction in the surface oxygen of the stoichiometric ceria (Ce^{4+}-O-Ce^{4+}) and non-stoichiometric ceria (Ce^{3+}-O-Ce^{4+}),[27,28] respectively. The peak at 712 ^oC can be assigned to the reduction of bulk ceria. For Ce/Ti-4 and Ce/Ti-3 catalyst, the intensity of bulk ceria peak is higher than that of surface oxygen reduction peaks, indicating the domination of lattice oxygen reduction for the catalyst. In contrast, Ce/Ti-2 and Ce/Ti-1 catalysts reveal lower-temperature at 400 and 484 ^oC due to surface oxygen reduction and a similar lattice oxygen reduction peak at 705 ^oC. However, the former one show much higher intensity than the latter one, implying that both catalysts contain more enriched surface active oxygen and Ce^{3+} chemical states in the catalyst. The above results indicate that the interaction between cerium oxide and nanorod TiO_2 plays a significant role in the reducibility of the catalysts, which could affect the activity of the samples in the NH_3-SCR reaction.

3.8. The results of XPS

XPS was conducted to identify the surface nature and atomic concentrate of various elements in the samples. Ce:Ti molar ratio to Ce/Ti catalyst (CeO_2 loading was 10 wt.%) stoichiometry is 0.05 in this work. As shown in Table 2, Ce:Ti molar ratio was 0.06 over Ce/Ti-2 catalyst, which was very close to its stoichiometry. Ce:Ti molar ratio was 0.18 and 0.19 over Ce/Ti-4 and Ce/Ti-3 catalysts, which was much higher than its stoichiometry, respectively. This implied a severe aggregation of CeO_2 phase on the catalyst surface. Combined with BET and SEM results, Ce/Ti-2 catalyst with 1 μm TiO_2 nanorod microspheres can not only provide suitable surface area for Ce loading, but also more readily contact between the support and active species compared with the other TiO_2 nanorod microspheres. Based on the above analysis, it can be concluded that Ce active species can be dispersed better on Ce/Ti-2 catalyst than on the other catalysts, which has also been confirmed by TEM results.

Fig. 9a shows XPS spectra of Ce 3d in Ce/Ti-*x* and Ce/P25 catalysts. The u_3, u_2, u, v_3, v_2, v peaks are attributed to Ce^{4+} chemical state while the u_1 and v_1 peaks are assigned to Ce^{3+} chemical state.[29] As a result, the chemical valence state of cerium on the surface of these cerium-containing samples is mainly +4, and a part of Ce^{3+} co-exists. The calculated percent content of Ce^{3+} for these cerium-containing samples is summarized in Table 2. The amounts of Ce^{3+} chemical state on Ce/Ti-2 catalyst surface (at 27.5%) are much higher than that on the other catalysts due to the stronger interactions between CeO_2 and TiO_2 on Ce/Ti-2. The presence of Ce^{3+} is generally accompanied with oxygen vacancies over TiO_2 support, thus Ce/Ti-2 catalyst is expected to possess abundant oxygen vacancies. Indeed, as shown in Fig. 9b and Table. 2, two peaks at 530.9-531.2 and 529.3-529.5 eV were observed over all samples, which could be attributed to lattice oxygen (denoted as O_β) and chemisorbed oxygen (denoted as O_α) on the catalyst surface.[30] It reveals that $O_\alpha/O_\alpha+O_\beta$ molar ratio in Ce/Ti-2 catalyst is much higher than that in the other catalysts, implying the presence of significant chemisorbed oxygen on the surface. Since such chemisorbed oxygen O_α is very beneficial to SCR process, it is unsurprising that Ce/Ti-2 catalyst exhibited the highest SCR activity among all catalysts.

Fig. 9c shows the XPS spectra of Ti 2p for Ce/Ti-2 and Ti-2 catalysts, where the peaks at ca. 458.8 eV and 464.6 eV are assigned to Ti2p$_{3/2}$ and Ti2p$_{1/2}$, respectively. Ce/Ti-2 catalyst revealed a lower binding energy shift fromTi-2 catalyst, indicating that there are some electron interactions between Ce^{4+} and Ti^{4+} in Ce/Ti-2 catalyst.

3.9. The results of Py-IR

The FTIR spectra of adsorbed pyridine were performed to study the acid properties of Ce/P25, Ce/Ti-2, P25 and Ti-2 samples. As shown in Fig. 10, the bands located at 1540 and 1640 cm^{-1} are assigned to pyridinium ions adsorbed on Brønsted sites. The bands located at 1440, 1455 and 1630 cm^{-1} are due to pyridinium ions adsorbed on Lewis sites.[3] The relative amount of Lewis acid sites over Ce/Ti-2, Ti-2, Ce/P25 and P25 samples are presented in Fig. 11. Only Lewis acid sites were observed in all samples at 200 ^{o}C. When the adsorption temperature was increased to 350 °C, the intensities of Lewis peaks decreased. It can be seen that Ce/P25 increases the Lewis acid sites concentration at 200 ^{o}C by 0.016 $\mu mol \cdot g^{-1}$ with respect to P25 support, while Ce/Ti-2 increases the Lewis acid sites concentration at 200 ^{o}C by 0.03 $\mu mol \cdot g^{-1}$ with respect to Ti-2 support. Therefore, it could be concluded that the more Lewis acid sites over Ce/Ti-2 catalyst would not be attributed to the addition of substance with abundant Lewis acid sites (the loadings of Ce are both 10 wt.%), but the changes in crystal structure and electron charge density caused by the generation of Ti-O-Ce mixed bonds. It has been reported that the acid sites may interact with the active components, and inhibit the agglomeration of the active components. Therefore, the abundant acid sites over Ce/Ti-2 catalyst may promote the dispersion of ceria species on support surface.

Ce/Ti-2 catalyst exhibited stronger CeO_2 and TiO_2 interactions, which inhibited the agglomeration of the formed oxide species during calcination. The observed catalytic activities were well correlated to the shape of TiO_2 support and the dispersion degree of CeO_2. Identical trend was also observed for NH_3-SCR activity, that was, Ce/Ti-2 > Ce/Ti-1 > Ce/Ti-3 > Ce/Ti-4. Moreover, the microspheres comprise nanorods with exposed {110} circumferential planes according to TEM, which indicates that {110} planes of rutile TiO_2 are the active surfaces. The morphology of nanoscale titania influences the synergistic interaction between CeO_2 and TiO_2 nanostructures. The existence of a large number of sharp edges and corners in the obtained 3D dendritic structures is extremely important for improving the catalytic performance of Ce/Ti-2 catalysts, which provide an appropriate surface area and copious active sites for reaction on the surfaces.[31,32] Compared with the nanorod microspheres with the size of 2-4 μm, almost no aggregation was observed on nanorod microspheres with 1 μm size and nanorods in the radial direction were highly dispersed. As a result, nanorod microspheres with 1 μm size seemed to take full advantage of nanorods with exposed {110} active plane, leading to the excellent performance of Ce/Ti-2 catalysts. Therefore, the shape of TiO_2 as the support is essentially important for obtaining high activity and selectivity through selective exposure of the reactive facets. Fortunately, nanorod microspheres with a suitable size of about 1 μm meeting NH_3-SCR demands were successfully synthesized by controlling the hydrolysis rates of titanium hydrate.

3.10. In-Situ DRIFTS Studies

3.10.1. Adsorption of NH_3

In-situ DRIFTS of NH_3 desorption over Ce/P25 and Ce/Ti-2 at different temperature is performed and the results are shown in Fig. 12. For Ce/P25 catalyst (Fig. 12a), several bands were detected in the range of 1100-1700 cm^{-1}. The bands at 1602 and 1164 cm^{-1} are attributed to the asymmetric and symmetric bending vibrations of N-H bond in NH_3 coordinately linked to Lewis acid site.[33,34] These adsorbed NH_3 species desorbed with further increasing of temperature, and disappeared completely at 350 ^{o}C. With regard to Ce/Ti-2 catalyst (Fig. 12b), similarly, the asymmetric and symmetric bending vibration of N-H bond in NH_3 coordinately linked to Lewis acid site can be observed at 1602, 1217 and 1161 cm^{-1}. Compared with Ce/P25 catalyst, the band for the symmetric bending vibration of N-H bon in NH_3 coordinately linked to lewis acid site (1217 cm^{-1}) appeared at 30 ^{o}C. One possible reason is that a strong interaction exits between CeO_2 and TiO_2 in Ce/Ti-2 catalyst, which leads to the stronger vibrations of N-H bond. Several new bands can be observed at 1550 and 1355 cm^{-1}.[35] The former one is attributed to the asymmetric bending vibration of N-H bond in $-NH_3^+$ group, which generates from the decomposition of NH_4^+ chemisorbed on Brønsted acid site. The latter one is related to scissoring and wagging vibrations of $-NH_2$ species, which is formed by hydrogen abstraction from NH_3 coordinated to Lewis acid site. Simultaneously, all the adsorbed NH_3 species on Lewis acid site disappeared completely at 300 ^{o}C owing to the decomposition and desorption of NH_3. The results show that the decomposition and desorption of the adsorbed NH_3 species on the surface of Ce/Ti-2 catalyst are easier due to the excellent oxygen storage capacity of CeO_2,[35] which is beneficial to the activation of NH_3 and the selective catalytic reduction of NO by NH_3.

3.10.2. Co-adsorption of NO and O_2

Fig. 13a shows *in-situ* DRIFTS of NO+O_2 on Ce/P25 in the temperature range of 30-350 ^{o}C. Several distinct bands appeared at 1633, 1603, 1579, 1288 and 1242 cm^{-1} at 30 ^{o}C, which are assigned to the asymmetric frequency of bridged nitrate (1633 and 1242 cm^{-1}), gaseous NO_2 molecules (1603 cm^{-1}), bidentate nitrate (1579 cm^{-1}), monodentate nitrate (1288 cm^{-1} and 1480 cm^{-1}), respectively.[36,37] The peaks attributed to the gaseous NO_2 molecules (1603 cm^{-1}) and monodentate nitrate (1288 cm^{-1}) disappeared completely with further increasing of temperature to 300 ^{o}C, indicating that these adsorbed NO species can be desorbed/decomposed/transformed during the heating process on the surface of Ce/P25. Moreover, the intensity of the band attributed to bidentate nitrate became weak with the elevation of temperature, but not disappeared even at 350 ^{o}C. Interestingly, the intensity of the peaks attributed to bridged nitrate (1633 and 1242 cm^{-1}) increased with further elevation of temperature firstly, and then decreased and not disappeared at 350 ^{o}C. The possible reason is that the transformation from monodentate nitrate or adsorbed NO species into bridged nitrate happened at low temperature on Ce/P25 catalyst. Fig. 13b shows the DRIFTS of NO_x adsorption over Ce/Ti-2 catalyst. Compared with Ce/P25 catalyst, the bands attributed to gaseous NO_2 molecules (1609 cm^{-1}) and bidentate nitrate (1575 cm^{-1}) were much stronger and the intensities of these bands kept high until 350 ^{o}C over Ce/Ti-2 catalyst. In contrast, the bands ascribed to bridged nitrate (1630 cm^{-1}) and monodentate nitrate (1298 cm^{-1} and 1475 cm^{-1}) over Ce/Ti-2 catalyst were much weaker than those on Ce/P25 catalyst. It was also observed that the bands attributed to monodenate nitrate (1298 cm^{-1} and 1475 cm^{-1}) appeared only at room temperature, while monodenate nitrate species is always thought to be detrimental to react with NH_3.[38] The formation of NO_2 and bidentate nitrate species is more evident on Ce/Ti-2 catalyst than that on Ce/P25 catalyst. This could be attributed to the presence of surface oxygen vacancies on Ce/Ti-2 catalyst.

3.10.3 Reaction between ammonia and adsorbed nitrogen oxides species

In-situ DRIFTS technique was employed to investigate the reaction between pre-adsorbed NO_x and NH_3 at 250 °C, and the corresponding results are displayed in Fig. 14. Switching the gas to NH_3 in 2 min led to the decrease of the intensities of adsorbed NO_2 (1604 cm^{-1}) and the disappearance of the band at 1579 cm^{-1} related to bidentate nitrate (Fig. 14a), indicating that these species are reactive in NH_3-SCR process. Simultaneously, the bands ascribed to the adsorbed NH_3 species appeared. Similar results were also observed for Ce/Ti-2 catalyst (See Fig. 14b). Both of the bands attributed to NO_2 (1603 cm^{-1}) and bidentate nitrate (1580 cm^{-1}) disappeared after NH_3 was passed over, confirming the involvements of NO_2 and bidentate nitrate species in the SCR reaction, and Fig. 13 shows that NO is readily adsorbed on Ce/Ti-2 catalyst and then oxidized into NO_2 and/or transferred to bidentate nitrate species, reacting with the adsorbed NH_3 to form N_2 an H_2O. The XPS results shows that Ce/Ti-2 catalyst is expected to possess abundant oxygen vacancies. Thus, it is speculated that the presence of abundant surface oxygen vacancies could facilitate the formation of NO_2 and bidentate nitrate species, leading to the remarkable excellent SCR performance for Ce/Ti-2 catalyst.

3.10.4 Reaction between nitrogen oxides and ammonia adspecies

Fig. 15 shows *in-situ* DRIFTS of Ce/P25 and Ce/T-2 catalysts as a function of time in a flow of NO + O_2 after the catalysts were pre-exposed to a flow of NH_3 for 60 min followed by N_2 purging for 30 min at 250 °C. As shown in Fig. 15a, the coordinated NH_3 on Lewis acid site (1195 and 1599 cm^{-1}) formed on Ce/P25 catalyst with feeding NH_3. When Ce/P25 catalyst was subsequently exposed to NO + O_2 afterwards, the intensities of all bands ammonia species decreased and the bands vanished in 5 min. Meanwhile, some bands attributed to NO_x species (1606, 1576, 1542 and 1229 cm^{-1}) appeared, suggesting that Lewis acid sites on Ce/P25 catalyst are involved in NH_3-SCR reaction. Similar results were also observed for Ce/Ti-2 catalyst (See Fig. 15b).It has been indicated that surface acidity plays an important role in the adsorption and activation of NH_3, and thus affects the occurrence of SCR reaction, especially at high temperature range.[17, 39] Therefore, the increased Lewis acid sites on Ce/Ti-2 catalyst should be an important reason for the enhanced catalytic activity, especially high temperature activity.

4. Conclusions

The novel size-tunable 3D rutile TiO_2 microspheres with nanorod building units were synthesized via a facile one-step hydrothermal synthesis method, based on a strategy of controlling the hydrolysis rate of the precursor. Ce/Ti-2 catalyst, which takes both advantages of good dispersion of CeO_2 by the size effect of TiO_2 support and enriched surface oxygen vacancies by a strong CeO_2-support interaction, exhibited high catalytic activity and strong SO_2 and H_2O resistance for NH_3-SCR reaction. In addition, the active NO_2 and bidentate nitrate species on Ce/Ti-2 catalyst are more easily formed compared with Ce/P25 catalyst. The successful synthesis of complex TiO_2 nanostructures supported CeO_2 catalysts via a controllable approach opens up a new way to improve NH_3-SCR performance of Ce/Ti-based catalysts.

Acknowledgements

This work was financially supported by the National Natural Science Foundation of China (21376261 and 21173270), 863 Program (2015AA034603 and 2013AA065302), the Beijing Natural Science Foundation (2142027), and the China University of Doctoral Selective Fund (20130007110007).

References

1 J.O. Barth, A. Jentys and J.A. Lercher, *Ind. Eng. Chem. Res.*, 2004, **43**, 3097-3104.

2 T. Zhang, J. Liu, D. Wang, Z. Zhao, Y. Wei, K. Cheng, G. Jiang and A. Duan, *Appl. Catal. B*, 2014, **148-149**, 520-531.

3 G. Busca, L. Lietti, G. Ramis and F. Berti, *Appl. Catal. B*, 1998, **18**, 1-36.

4 P. Forzatti, *Appl. Catal. A*, 2001, **222**, 221-236.

5 S. Roy, M.S. Hegde and G. Madras, *Appl. Energy.*, 2009, **86**, 2283-2297.

6 G. Carja, Y. Kameshima, K. Okada and C.D. Madhusoodana, *Appl. Catal. B*, 2007, **73**, 60-64.

7 H. Sjövall, L. Olsson, E. Fridell and R.J. Blint, *Appl. Catal. B*, 2006, **64**, 180-188.

8 F. Can, S. Berland, S. Royer, X. Courtois and D. Duprez, *ACS Catal.*, 2013, **3**, 1120-1132.

9 Y. Li, H. Cheng, D. Li, Y. Qin, Y. Xie and S. Wang, *Chem. Commun.*, 2008, 1470-1472.

10 L. Chen, J. Li, W. Ablikim, J. Wang, H. Chang, L. Ma, J. Xu, M. Ge and H. Arandiyan, *Catal. Lett.*, 2011, **141**, 1859-1864.

11 W. Shan, F. Liu, H. He, X. Shi and C. Zhang, *Chem. Commun.*, 2011, **47**, 8046-8048.

12 G.S. Qi and R.T. Yang, *Chem. Commun.*, 2003, 848-849.

13 F. Liu and H. He, *Catal. Today*, 2010, **153**, 70-76.

14 F. Liu, H. He, C. Zhang, Z. Feng, L. Zheng, Y. Xie and T. Hu, *Appl. Catal. B*, 2010, **96**, 408-420.

15 W. Xu, Y. Yu, C. Zhang and H. He, *Catal. Commun.*, 2008, **9**, 1453-1457.

16 W. Xu, H. He and Y. Yu, *J. Phys. Chem. C*, 2009, **113**, 4426-4432.

17 W. Shan, F. Liu, H. He, X. Shi and C. Zhang, *Appl. Catal. B*, 2012, **115-116**, 100-106.

18 R. Jin, Y. Liu, Y. Wang, W. Cen, Z. Wu, H. Wang and X. Weng, *Appl. Catal. B*, 2014, **148-149**, 582-588.

19 Y. Shen, Y. Ma and S. Zhu, *Catal. Sci. Technol.*, 2012, **2**, 589-599.

20 Y. Liu, W. Yao, X. Cao, X. Weng, Y. Wang, H. Wang and Z. Wu, *Appl. Catal. B*, 2014, **160-161**, 684-691.

21 K.A. Michalow-Mauke, Y. Lu, K. Kowalski, T. Graule, M. Nachtegaal, O. Kröcher and D. Ferri, *ACS Catal.*, 2015, **5**, 5657-5672.

22 X. Chen, H. Wang, Z. Wu, Y. Liu and X. Weng, *J. Phys. Chem. C*, 2011, **115**, 17479-17484.

23 J. Nian, S. Chen, C. Tsai and H. Teng, *J. Phys. Chem. B*, 2006, **110**, 25817-25824.

24 R. Gao, D. Zhang, X. Liu, L. Shi, P. Maitarad, H. Li, J. Zhang and W. Cao, *Catal. Sci. Technol.*, 2013, **3**, 191-199.

25 Y. Rui, Y. Li, Q. Zhang and H. Wang, *Nanoscale*, 2013, **5**, 12574-12581.

26 A.C. Johnston-Peck, S.D. Senanayake, J.J. Plata, S. Kundu, W. Xu, L. Barrio, J. Graciani, J.F. Sanz, R.M. Navarro, J.L.G. Fierro, E.A. Stach and J.A. Rodriguez, *J. Phys. Chem. C*, 2013, **117**, 14463-14471.

27 S. Damyanova, C.A. Perez, M. Schmal and J.M.C. Bueno, *Appl. Catal. A*, 2002, **234**, 271-280.

28 B. Murugan and A.V. Ramaswamy, *J. Phys. Chem. C*, 2008, **112**, 20429-20442.

29 M.S.P. Francisco, V.R. Mastelaro, P.A.P. Nascente and A.O. Florentino, *J. Phys. Chem. B*, 2001, **105**, 10515-10522.

30 K. Cheng, J. Liu, T. Zhang, J. Li, Z. Zhao, Y. Wei, G. Jiang and A. Duan, *J. Environ. Sci.*, 2014, **26,** 2106-2113.

31 Z. Sun, J.H. Kim, Y. Zhao, F. Bijarbooneh, V. Malgras, Y. Lee, Y.M. Kang and S.X. Dou, *J. Am. Chem. Soc.*, 2011, **133**, 19314-19317.

32 J.Y. Liao, B.X Lei, D.B. Kuang and C.Y. Su, *Energy Environ. Sci.*, 2011, **4**, 4079-4085.

33 L. Lietti, I. Nova, G. Ramis, L. Dalllacqua, G. Busca, E. Giamello, P. Forzatti and F. Bregani, *J. Catal.*, 1999, **187**, 419-435.

34 P.G. Smirniotis, D.A. Peña and B.S. Uphade, *Angew. Chem. Int. Ed*, 2001, **40**, 2479-2482.

35 X. Yao, L. Zhang, L. Li, L. Liu, Y. Cao, X. Dong, F. Gao, Y. Deng, C. Tang, Z. Chen, L. Dong and Y. Chen, *Appl. Catal. B*, 2014, **150-151**, 315-329.

36 Z. Liu, J. Zhu, J. Li, L. Ma and S.I. Woo, *ACS Appl. Mater. Inter.*, 2014, **6**, 14500-14508.

37 Z. Wu, B. Jiang, Y. Liu, H. Wang and R. Jin, *Environ. Sci. Technol.*, 2007, **41**, 5812-5817.

38 W.S. Kijlstra, D.S. Brands, H.I. Smit, E.K. Poels and A. Bliek, *J. Catal.*, 1997, **171**, 219-230.

39 F. Guo, J. Yu, M. Chu and G. Xu, *Catal. Sci. Technol.*, 2014, **4**, 2147-2155.

Table captions

Table 1 The textural and structural properties of all catalysts

Table 2 The quantitative results of the mole ratio of different atoms by XPS and peak-fitting results of Ce 3d and O 1s spectra of Ce/Ti-*x* and Ce/P25 catalysts

Table 1

The textural and structural properties of all catalysts

Samples	S_{BET} [a] ($m^2 \cdot g^{-1}$)	V_{mic} [b] ($cm^3 \cdot g^{-1}$)
Ce/Ti-1	49.1	0.203
Ce/Ti-2	45.2	0.258
Ce/Ti-3	34.7	0.126
Ce/Ti-4	32.6	0.138
Ce/P25	44.5	0.35

[a] Calculated by BET method

[b] Calculated by *t*-plot method

Table 2

The quantitative results of the mole ratio of different atoms by XPS and peak-fitting results of Ce 3d and O 1s spectra of Ce/Ti-*x* and Ce/P25 catalysts

Catalysts	Surface composition/ mol.%			Atomic ratio/%		
	O	Ti	Ce	Ce/Ti	Ce^{3+}/ (Ce^{3+}+ Ce^{4+})	$O_{\alpha}/(O_{\alpha}+O_{\beta})$
Ce/Ti-1	69.88	27.44	2.69	0.1	29.5	18.7
Ce/Ti-2	68.65	29.36	1.99	0.06	38.8	27.5
Ce/Ti-3	69.82	25.66	4.52	0.18	28.3	15.1
Ce/Ti-4	70.12	25.03	4.86	0.19	19.9	11
Ce/P25	69.83	26.95	3.23	0.12	32	20.8

Figure captions

Fig. 1. Schematic illustration of the formation of hierarchical TiO_2 nanorod microspheres.

Fig. 2. NO_x conversion (a) and N_2 selectivity (b) as a function of reaction temperature over Ce/P25 and Ce/Ti-*x* catalysts. Reaction conditions: [NO] = [NH_3] = 1000 ppm, [O_2] = 3%, balance N_2, total gas flow rate 500 ml/min, and GHSV = 50,000 h^{-1}.

Fig. 3. NO_x conversion as a function of time over Ce/Ti-2 and Ce/P25 catalysts at 300 ^{o}C in the presence of 5% H_2O (a), NO_x conversion as a function of time over Ce/Ti-2 and Ce/P25 catalysts at 300 ^{o}C in the presence of 100 ppm SO_2 (b), NO_x conversion as a function of time over Ce/Ti-*x* and Ce/P25 catalysts at 300 ^{o}C in the presence of 5% H_2O and 100 ppm SO_2 (c).

Fig. 4. X-ray diffraction patterns of Ce/Ti-*x* catalysts.

Fig. 5. Nitrogen adsorption-desorption isotherms of Ce/P25 and Ce/Ti-*x* catalysts.

Fig. 6. SEM images of Ce/Ti-*x* catalysts : (a_1-a_3) Ce/Ti-1, (b_1-b_3) Ce/Ti-2, (c_1-c_3) Ce/Ti-3, (d_1-d_3) Ce/Ti-4 and (e) SEM image and EDX analyses for Ce/Ti-2 catalyst.

Fig. 7. TEM and HRTEM images of Ce/Ti-2 (a-f); EDX mapping images of (g) Ce/Ti-2 and (h) Ce/P25 catalysts.

Fig. 8. H_2-TPR profiles of Ce/Ti-*x* catalysts.

Fig. 9. XPS spectra of (a) Ce 3d, (b) O 1s and (c) Ti 2p in Ce/Ti-*x* and Ce/P25 catalysts.

Fig. 10. FT-IR spectra of pyridine adsorbed on Ce/P25, Ce/Ti-2, P25 and Ti-2 samples after degassing at 200 ^{o}C and 350 ^{o}C.

Fig. 11. Surface Lewis acid sites per gram at 200 ^{o}C over Ce/P25, Ce/Ti-2, P25 and Ti-2 samples.

Fig. 12. *In-situ* DRIFTS of NH_3 desorption on Ce/P25(a) and Ce/Ti-2(b) measured at 30-350 ^{o}C.

Fig. 13. *In-situ* DRIFTS of NO+O_2 desorption on Ce/P25(a) and Ce/Ti-2(b) measured at 30-350 ^{o}C.

Fig. 14. *In-situ* DRIFTS over Ce/P25(a) and Ce/Ti-2(b) as a function of time in a flow

of NH_3 after the catalysts was pre-exposed to a flow of NO + O_2 for 60 min followed by N_2 purging for 30 min at 250 ^oC.

Fig. 15. *In-situ* DRIFTS over Ce/P25(a) and Ce/Ti-2(b) as a function of time in a flow of NO + O_2 after the catalysts was pre-exposed to NH_3 a flow of for 60 min followed by N_2 purging for 30 min at 250 ^oC.

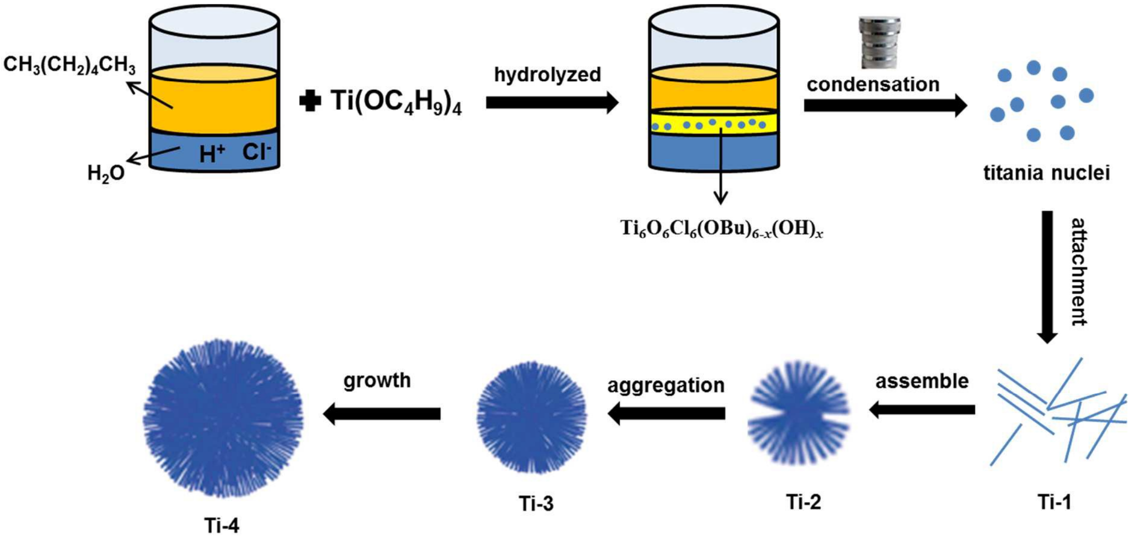
$CH_3(CH_2)_4CH_3$
H⁺ Cl⁻
H_2O
+ $Ti(OC_4H_9)_4$
hydrolyzed
$Ti_6O_6Cl_6(OBu)_{6-x}(OH)_x$
condensation
titania nuclei
attachment
Ti-1
assemble
Ti-2
aggregation
Ti-3
growth
Ti-4

Fig. 1.

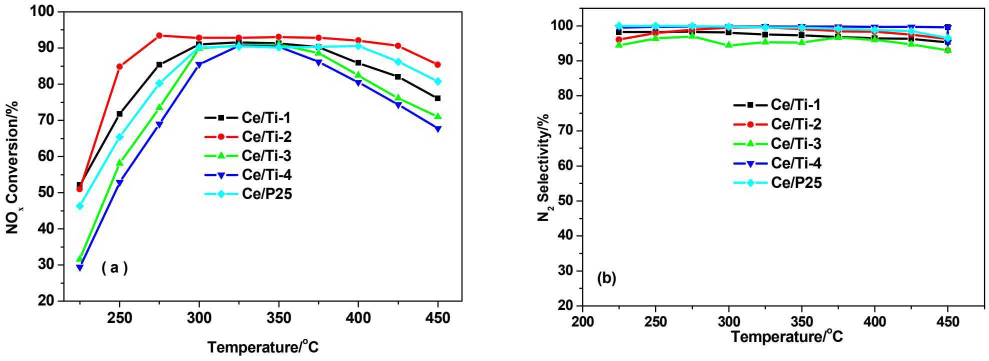
NO$_x$ Conversion/%
100
90
80
70
60
50
40
30
20
250
300
350
400
450
Temperature/°C
Ce/Ti-1
Ce/Ti-2
Ce/Ti-3
Ce/Ti-4
Ce/P25
(a)
N$_2$ Selectivity/%
100
90
80
70
60
50
40
30
20
200
250
300
350
400
450
Temperature/°C
Ce/Ti-1
Ce/Ti-2
Ce/Ti-3
Ce/Ti-4
Ce/P25
(b)

Fig. 2.

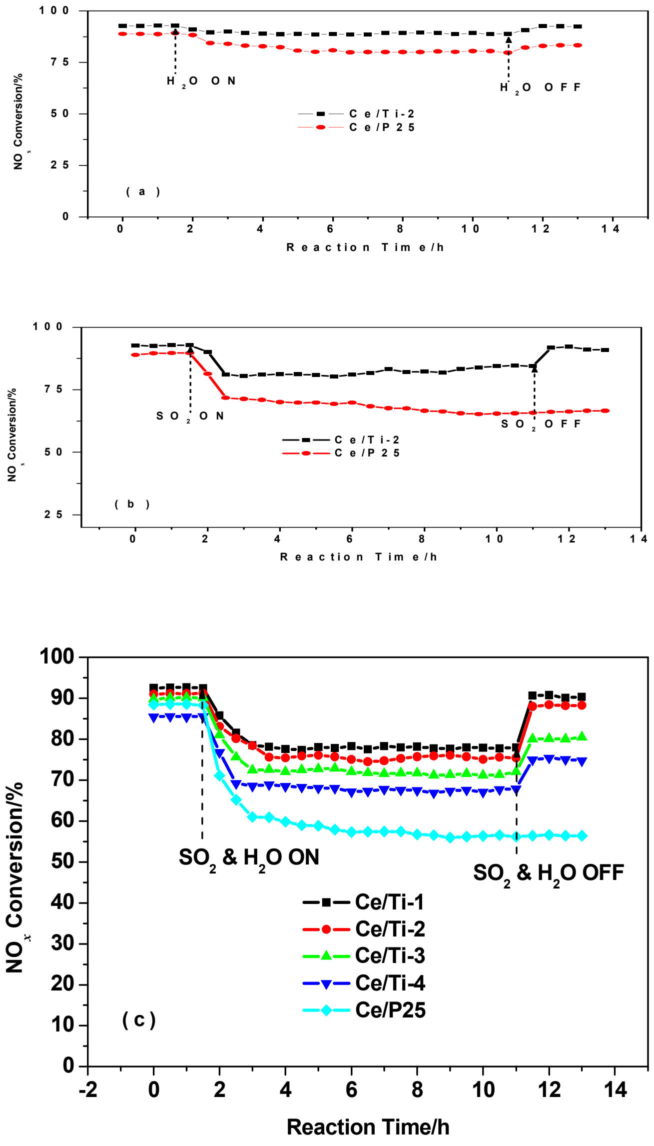
100
75
50
25
0
NOx Conversion/%
H2O ON
H2O OFF
Ce/Ti-2
Ce/P25
(a)
0 2 4 6 8 10 12 14
Reaction Time/h
100
75
50
25
NOx Conversion/%
SO2 ON
SO2 OFF
Ce/Ti-2
Ce/P25
(b)
0 2 4 6 8 10 12 14
Reaction Time/h
100 90 80 70 60 50 40 30 20 10 0
NOx Conversion/%
SO2 & H2O ON
SO2 & H2O OFF
Ce/Ti-1
Ce/Ti-2
Ce/Ti-3
Ce/Ti-4
Ce/P25
(c)
-2 0 2 4 6 8 10 12 14
Reaction Time/h

Fig. 3.

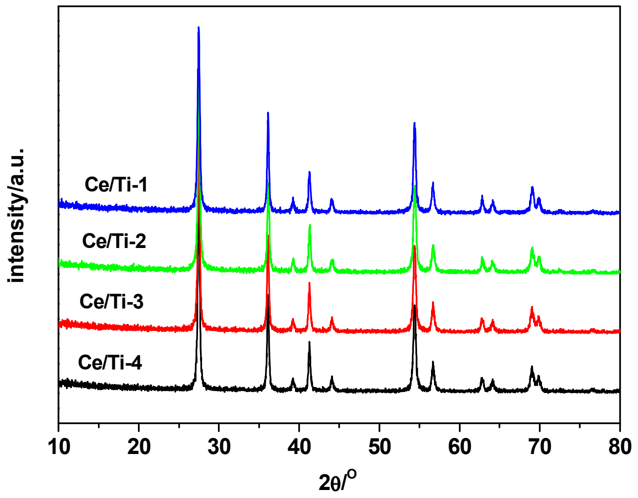

Fig. 4.

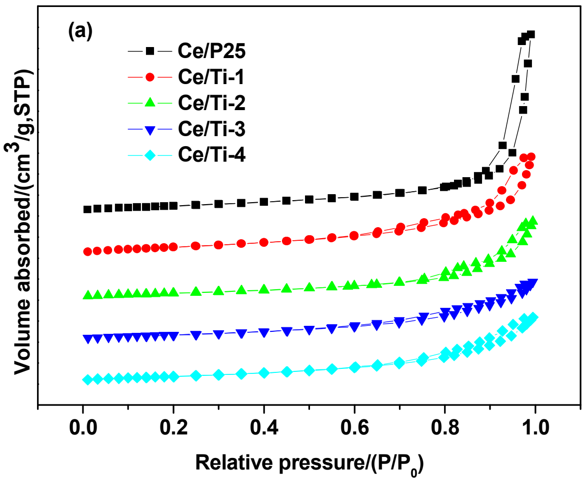
(a)
Ce/P25
Ce/Ti-1
Ce/Ti-2
Ce/Ti-3
Ce/Ti-4
Volume absorbed/(cm^3/g,STP)
0.0
0.2
0.4
0.6
0.8
1.0
Relative pressure/(P/P$_0$)

Fig. 5.

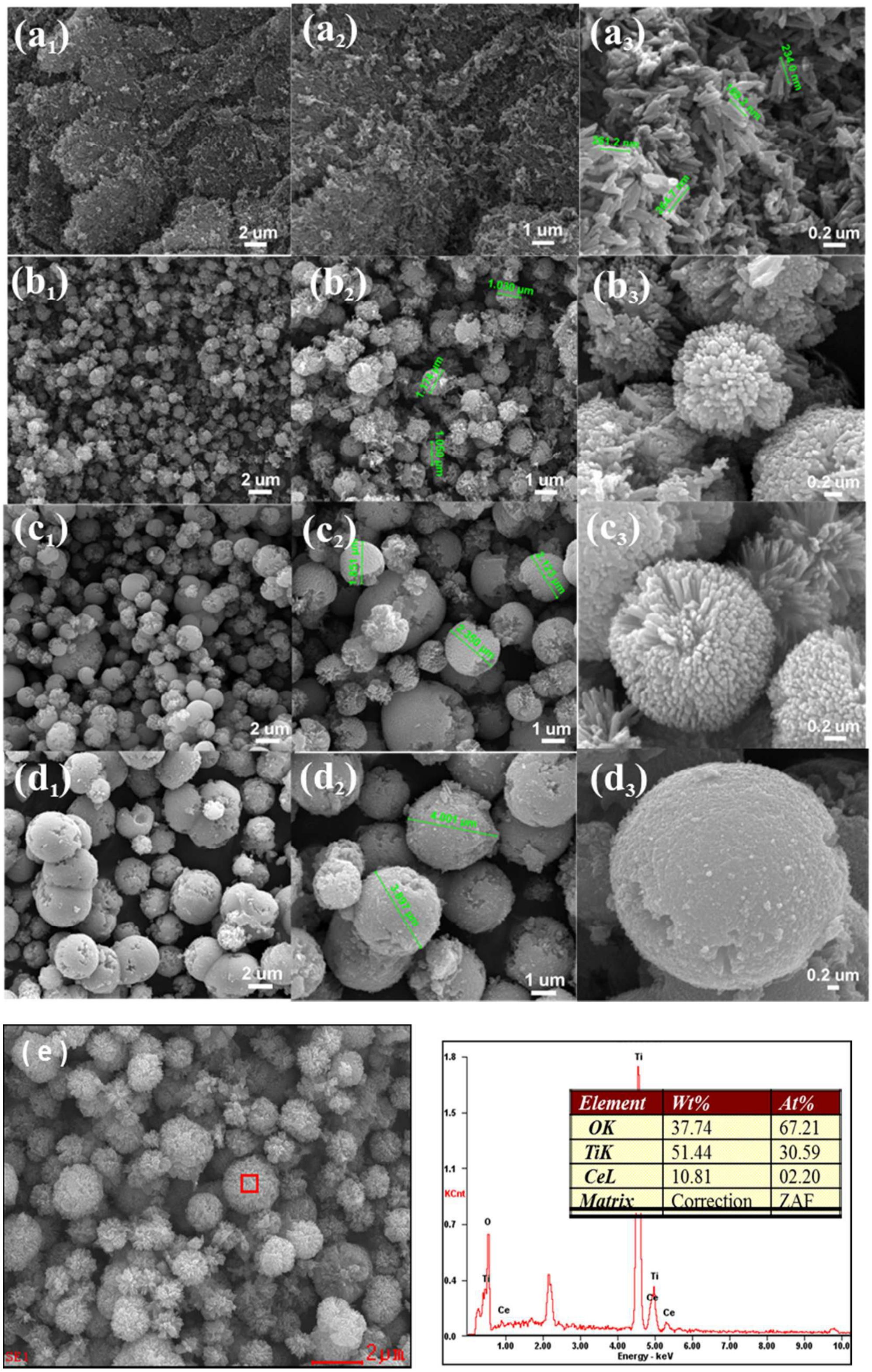

Element	Wt%	At%
OK	37.74	67.21
TiK	51.44	30.59
CeL	10.81	02.20
Matrix	Correction	ZAF

Fig. 6.

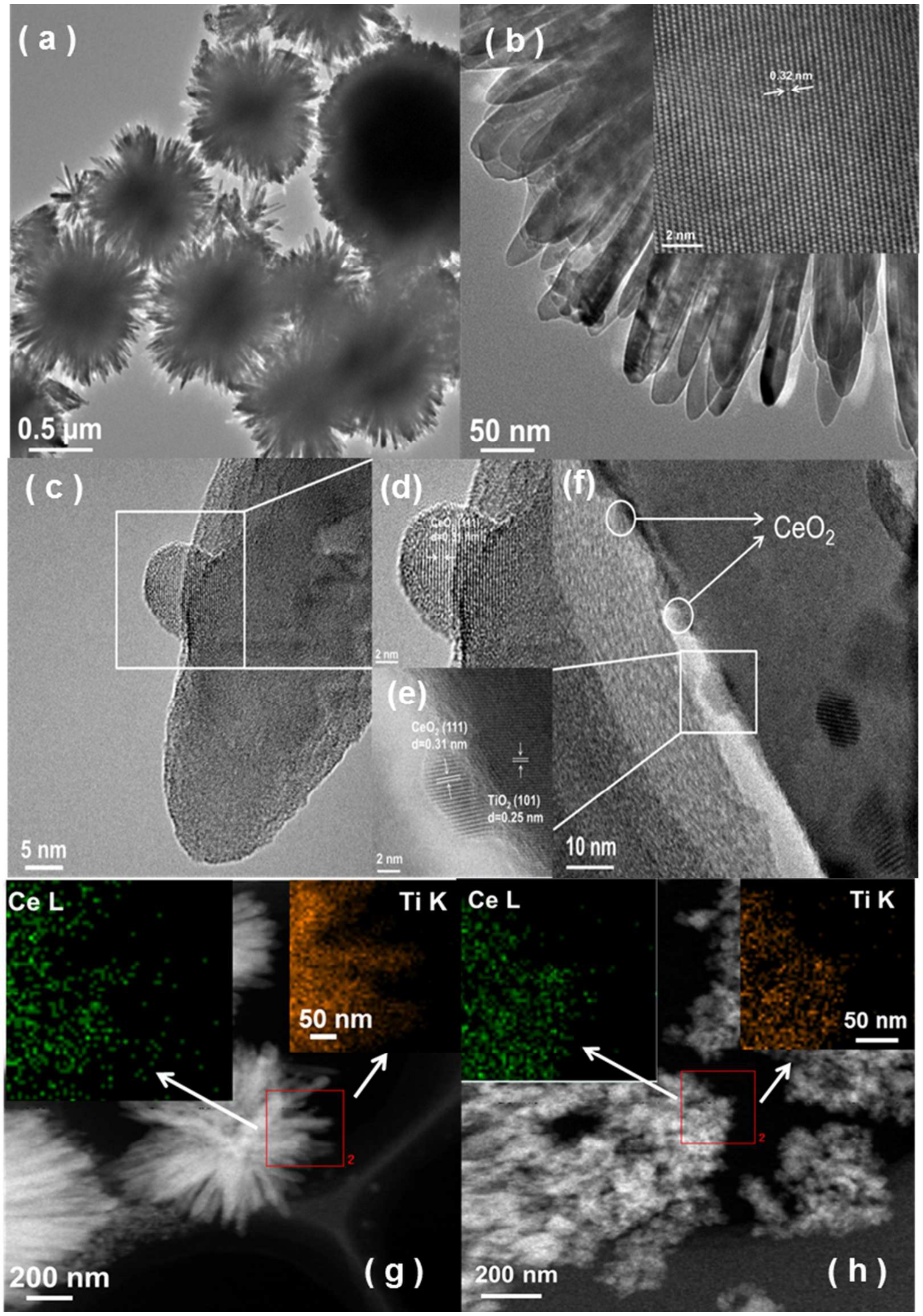
(a)
0.5 µm
(b)
0.32 nm
2 nm
50 nm
(c)
5 nm
(d)
CeO₂ (111) d=0.31 nm
2 nm
(e)
CeO₂ (111) d=0.31 nm
TiO₂ (101) d=0.25 nm
2 nm
(f)
CeO₂
10 nm
Ce L
Ti K
50 nm
200 nm
(g)
Ce L
Ti K
50 nm
200 nm
(h)

Fig. 7.

585

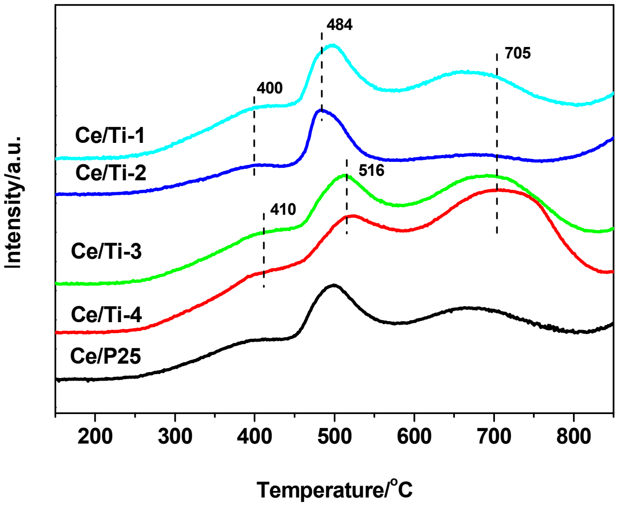

586

587 Fig. 8.

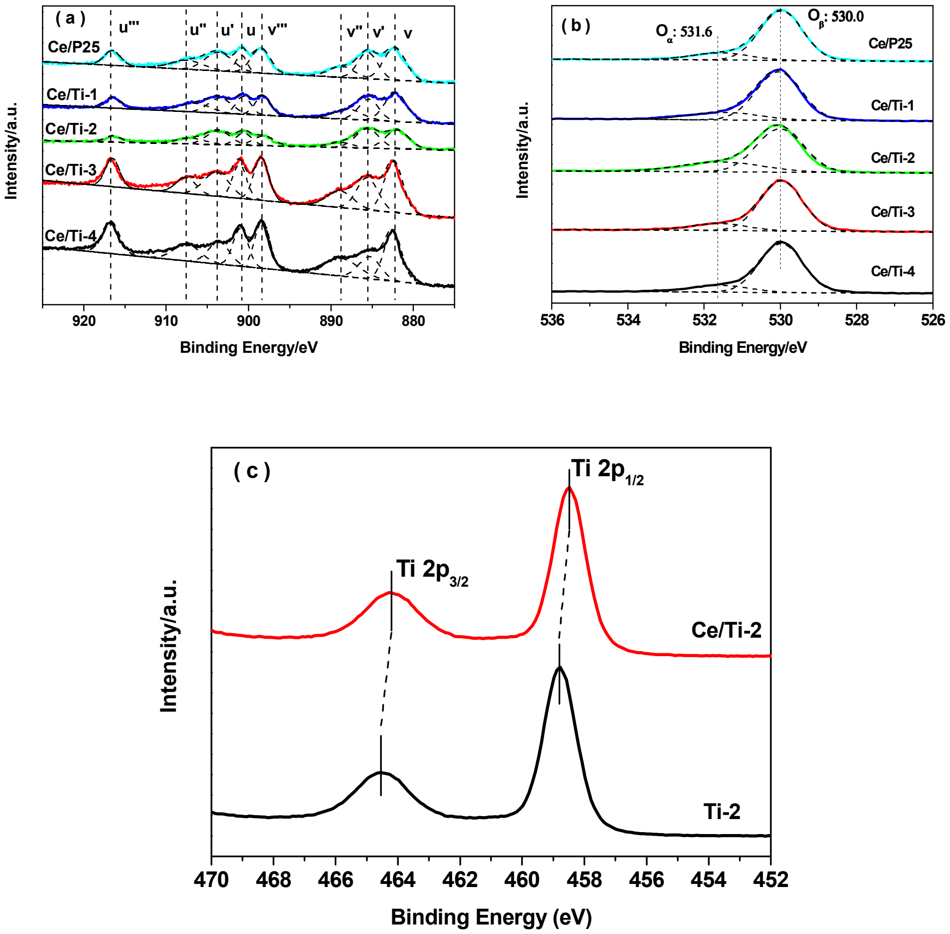
(a)
u'''
u''
u'
u
v'''
v''
v'
v
Ce/P25
Ce/Ti-1
Ce/Ti-2
Ce/Ti-3
Ce/Ti-4
Intensity/a.u.
920
910
900
890
880
Binding Energy/eV
(b)
O$_\alpha$: 531.6
O$_\beta$: 530.0
Ce/P25
Ce/Ti-1
Ce/Ti-2
Ce/Ti-3
Ce/Ti-4
Intensity/a.u.
536
534
532
530
528
526
Binding Energy/eV
(c)
Ti 2p$_{1/2}$
Ti 2p$_{3/2}$
Ce/Ti-2
Ti-2
Intensity/a.u.
470
468
466
464
462
460
458
456
454
452
Binding Energy (eV)

Fig. 9.

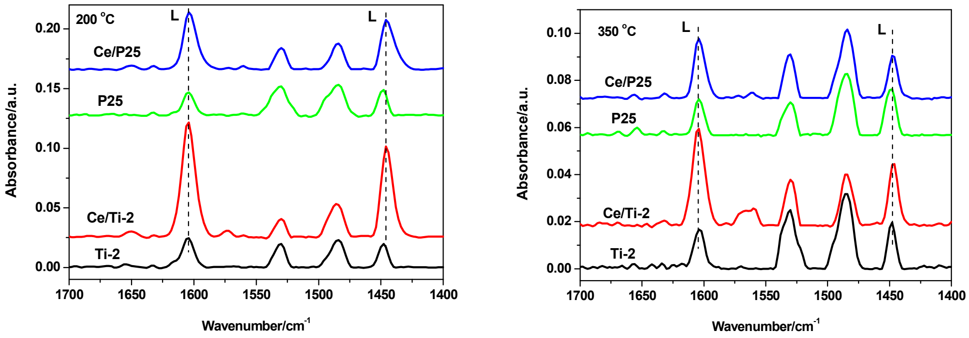
200 °C
L
L
Ce/P25
P25
Ce/Ti-2
Ti-2
Absorbance/a.u.
0.20
0.15
0.10
0.05
0.00
1700
1650
1600
1550
1500
1450
1400
Wavenumber/cm^{-1}
350 °C
L
L
Ce/P25
P25
Ce/Ti-2
Ti-2
Absorbance/a.u.
0.10
0.08
0.06
0.04
0.02
0.00
1700
1650
1600
1550
1500
1450
1400
Wavenumber/cm^{-1}

Fig. 10.

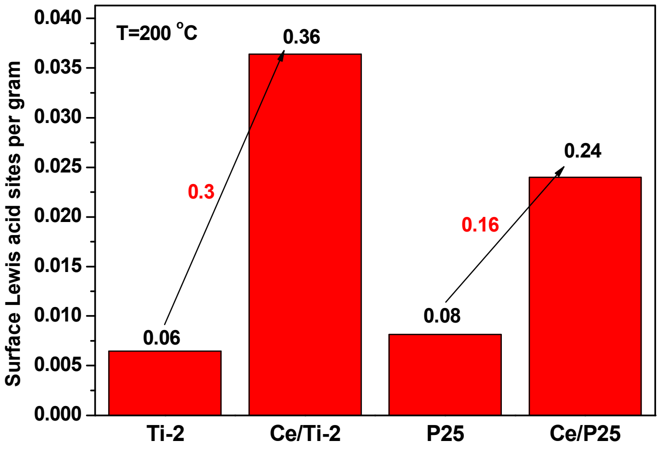

593

594 Fig. 11.

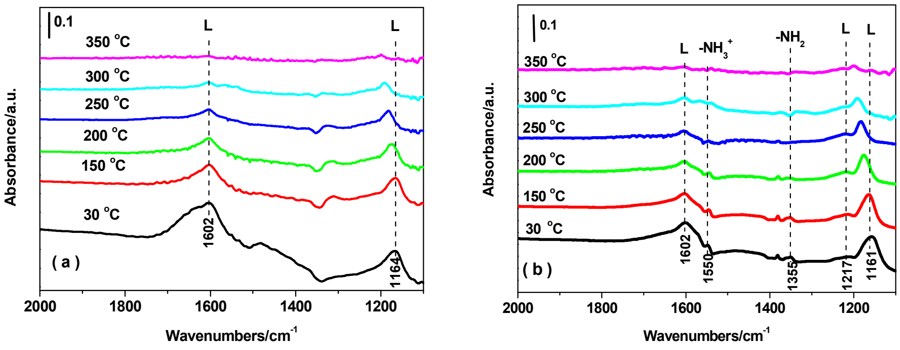
0.1
L
L
350 °C
300 °C
250 °C
200 °C
150 °C
30 °C
1602
1164
(a)
Absorbance/a.u.
2000
1800
1600
1400
1200
Wavenumbers/cm-1
0.1
L
-NH3+
-NH2
L
L
350 °C
300 °C
250 °C
200 °C
150 °C
30 °C
1602
1550
1355
1217
1161
(b)
Absorbance/a.u.
2000
1800
1600
1400
1200
Wavenumbers/cm-1

Fig. 12.

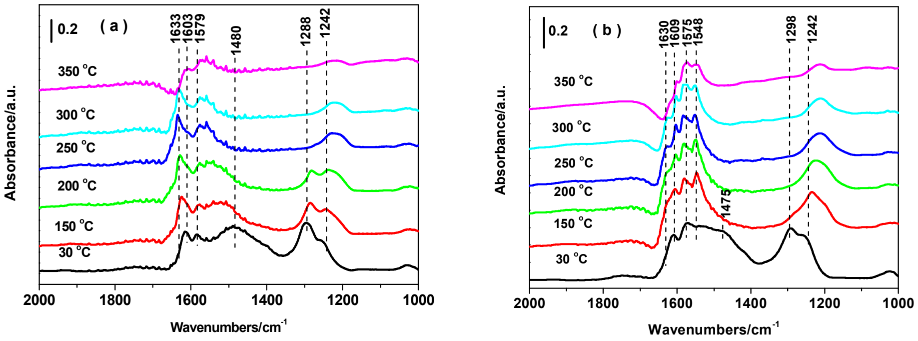
0.2
(a)
1633
1603
1579
1480
1288
1242
350 °C
300 °C
250 °C
200 °C
150 °C
30 °C
Absorbance/a.u.
2000
1800
1600
1400
1200
1000
Wavenumbers/cm-1
0.2
(b)
1630
1609
1575
1548
1475
1298
1242
350 °C
300 °C
250 °C
200 °C
150 °C
30 °C
Absorbance/a.u.
2000
1800
1600
1400
1200
1000
Wavenumbers/cm-1

Fig. 13.

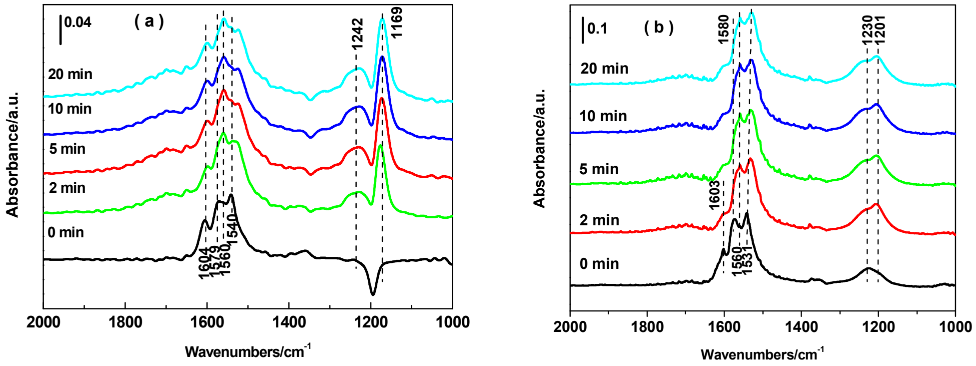
0.04
(a)
20 min
10 min
5 min
2 min
0 min
1604
1579
1560
1540
1242
1169
Absorbance/a.u.
2000
1800
1600
1400
1200
1000
Wavenumbers/cm-1
0.1
(b)
1580
1230
1201
20 min
10 min
5 min
2 min
0 min
1603
1560
1531
Absorbance/a.u.
2000
1800
1600
1400
1200
1000
Wavenumbers/cm-1

Fig. 14.

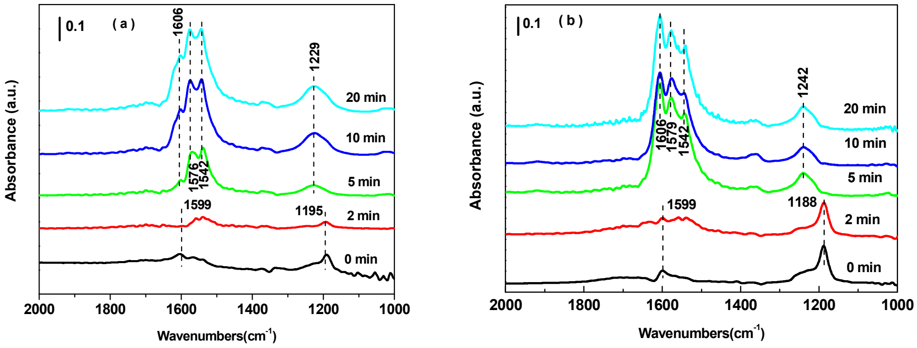
0.1
(a)
1606
1576
1542
1229
1599
1195
20 min
10 min
5 min
2 min
0 min
Absorbance (a.u.)
2000
1800
1600
1400
1200
1000
Wavenumbers(cm^{-1})
0.1
(b)
1606
1579
1542
1242
1599
1188
20 min
10 min
5 min
2 min
0 min
Absorbance (a.u.)
2000
1800
1600
1400
1200
1000
Wavenumbers(cm^{-1})

Fig. 15.

Graphical Abstract

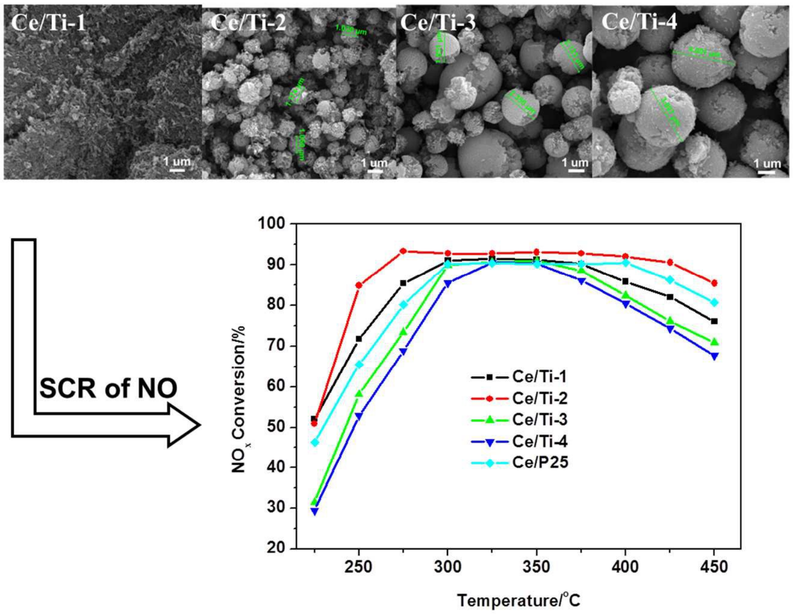

Morphology and structure of TiO_2 supports impact NH_3-SCR performance of Ce/Ti catalysts significantly